OPTICAL REVIEW Vol. 15, No. 2 (2008) 1–8

脚注の郵便番号をご確認ください。
Table4の引用がありません。

OR PROOF

Rotation Rate of a Three-Wing Rotor Illuminated by Upward-Directed Focused Beam in Optical Tweezers

Hiroo UKITA*, Takakazu OHNISHI†, and Yasunari NONOHARA‡

Faculty of Science and Engineering, Ritsumeikan University, 1-1-1 Nojihigashi, Kusatsu, Shiga 525-8677, Japan

(Received August 31, 2007; Accepted December 17, 2007)

The optical torque and the trapping position (focal point) in optical tweezers are analyzed for upward-directed focused laser illumination using a ray optics model, considering that laser light is incident at not only the lower surface but also the side surface of a 3-wing rotor. The viscous drag force due to the pressure and the shearing stress on all surfaces of the rotor is evaluated using computational fluid dynamics. The rotation rate is simulated in water by balancing the optical torque with the drag force, resulting in 500 rpm for an SU-8 rotor with 20 μm diameter at a laser power of 200 mW. The trapping position is estimated to be 7.6 μm in the rotor with an upward-directed laser at 200 mW via an objective lens having a numerical aperture of 1.4. Both the rotation rate and the trapping position agree well with the values obtained in the experiment.

Key words: optical tweezers, optical torque, trapping position, drag force, rotation rate, rotor, upward-directed focused beam

1. Introduction

Many kinds of applications using optical trapping[1–4] and optical rotation[5–8] have been proposed. Possible micro electro mechanical system (MEMS) applications include actuators for vibration,[6] mixing[7] and pumping,[8] some of which will be used to control a microliquid in future lab-on-a-chip devices.[9]

Optical rotation is possible by the transfer of the photon spin angular momentum[10] with circular polarization, by the orbital angular momentum[11] with a Laguerre-Gauss beam, and by the optical pressure exerted on a dissymmetrically shaped object.[12] It is estimated that the torque due to the optical pressure on a dissymmetrical shape will be one order of magnitude greater than those due to the spin angular momentum and the orbital angular momentum.

Dissymmetrical rotors with a simple shuttlecock structure,[13] a complicated structure,[14] and a slope structure[15] have been proposed, fabricated and demonstrated. The rotors are aligned and rotated with the light beam propagation axis using optical tweezers. Among such rotors, a 3-wing shuttlecock rotor is easy to fabricate in the correct shape, stable in trapping and fast in rotation.[16] In the conventional optical torque analysis, the trapping position is outside the rotor, but the position was found to be in the rotor in an experiment (see Appendix) with upward-directed focused laser illumination.[16]

In this paper, light-driven 3-wing rotors are analyzed to obtain both the optical torque and the trapping position, which depend on the laser power, using a ray optics model. The drag force is also analyzed by computational fluid dynamics (CFD) to evaluate the rotation rate. Enhanced shapes with various wing widths and wing angles are demonstrated.

*E-mail address: ukita@se.ritsumei.ac.jp
†Present address: Kansai Electric Power Corporation, Nakanoshima, Osaka 530-XX XX, Japan.
‡Present address: Ishida Corporation, Rittoh, Shiga 520-XX XX, Japan.

2. Analysis of Optical Torque

2.1 *Analysis method: Upward-directed focused beam illumination*

We employ an upward-directed beam configuration because it requires a less trapping power than that of a downward-directed one, because axial trapping force is equivalent to $F_g + F_s$ for upward illumination but to $F_g - F_s$ for downward illumination, where F_g is the gradient force and F_s is the scattering force exerted on the rotor.[17] Figure 1 shows a 3-wing shuttlecock rotor, the lower surface of which is illuminated by an upward-directed focused laser beam. When the trapping position is outside the rotor, all the incident lights are refracted at the lower surface.

In the figure, when the incident light is refracted at the lower surface, the momentum changes and downward optical pressure force is exerted, but when the laser light is transmitted from the upper surface, upward optical pressure is exerted, lifting the rotor. An optical pressure is also exerted when the light is transmitted from the side surfaces. The optical pressure F is exerted on side surfaces A and B but not on side surface C, because surface C is parallel to the radial direction and does not transmit light. When light is transmitted from side surface B, it does not contribute to the torque because its direction is radial. Therefore, the torque, which rotates the rotor counterclockwise, originates only from the optical pressure on side surface A.

We define the optical torque M_1 as that generated when the incident light enters the lower surface and then is transmitted from the side surface. The uniformly filled laser beam was divided into 100 (radial direction) × 400 (angle direction) elements on the objective lens aperture. We considered a ray incident on the lens and estimated the torque at point (r_L, α) on side surface A. The radius r_L is expressed as

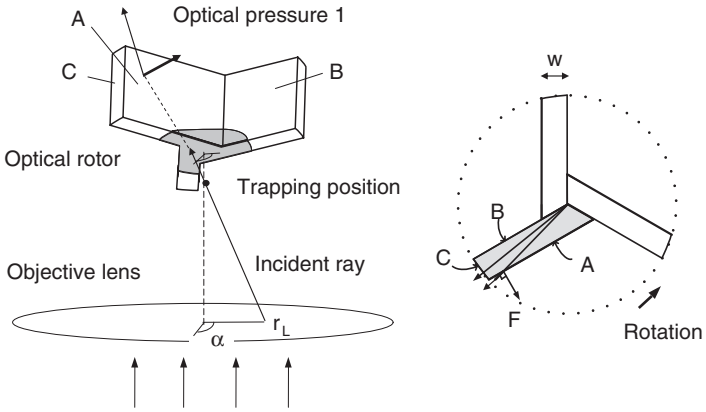

Fig. 1. Optical torque analysis for a 3-wing optical rotor. Ray tracing and optical torque M_1 exerted on a rotor illuminated upwards by a focused beam. The incident light enters the lower surface and is transmitted from the side surface.

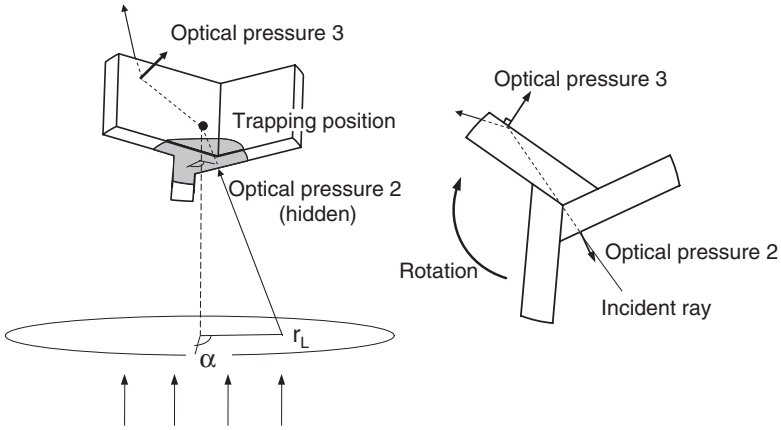

Fig. 2. Optical torque M_2 exerted when incident light enters the side surface and optical torque M_3 exerted when the light is transmitted from another wing side surface.

$$r_{\mathrm{L}} = \frac{w}{\cos\alpha}, \tag{1}$$

where w is the wing width. Optical pressure F exerted at the incident light angle of θ_1 is expressed as[17)]

$$F = \frac{n_1}{c_0} P\left[(1+R)\cos\theta_1 - \frac{n_2}{n_1} T\cos\theta_2\right], \tag{2}$$

where n_1 and n_2 are the refractive index of the surrounding medium and that of the rotor, respectively. P is the laser power, c_0 is the speed of light in a vacuum, and θ_2 is the refractive angle obtained from Snell's law. R and T are the reflectivity and transmissivity and they are derived from the Fresnel formula. As a consequence, optical pressure F can be calculated if the incident light angle θ_1 is defined.

The optical torque M_1 exerted on the 3 wing surfaces is

$$M_1 = 3\int_0^{\cos^{-1}(2w/d)} \int_{r_{L_{\min}}}^{r_{L_{\max}}} Fr^2 dr\, d\alpha, \tag{3}$$

where d is the rotor diameter and $r_{L_{\min}}$ and $r_{L_{\max}}$ are the minimum and maximum distances from the optical axis, respectively. They are given as $r_{L_{\min}} = 0$ and $r_{L_{\max}} = \tan\arcsin(NA/n_1)$.

2.2 Effect of light incident at the side surface

When the trapping position (focal point) is in the rotor, the outer part of the laser light is incident at the side surface, exerts optical pressure 2 (torque M_2), and is transmitted from the side surface of another wing where it exerts optical pressure 3 (torque M_3), as illustrated in Fig. 2. Figure 3 shows the optical torque dependence on the trapping position, with torques M_1, M_2, and M_3, and total torque $M_{\mathrm{total}}{}^{\mathrm{opt}}$ as parameters, estimated for the SU-8 rotor under the conditions listed in Table 1. It is found that as the trapping position becomes a more negative value (deeper in the rotor), the optical torque M_3 increases rapidly and comes to play an important role. Also, the total optical torque $M_{\mathrm{total}}{}^{\mathrm{opt}} = M_1 + M_2 + M_3$ varies with the trapping position, which depends on the laser power.

Figure 4 shows the total torque dependence on the trapping position with wing width w as a parameter. The torque is large for a narrow wing when the trapping position is in the rotor, but it is large for a wide wing when the trapping position is outside the rotor.

Figure 5 shows the total torque dependence on the trapping position with wing angle β as a parameter. The torque is large at a wing angle less than 90°, which occurs when the trapping position is in the rotor, but it is large at a wing angle greater than 90° when the trapping position is outside the rotor.

3. Analysis of Trapping Position

3.1 Analysis method: Balancing trapping force with weight in the medium

When light is incident at the lower surface of a rotor, downward optical pressure force F_1 is exerted, but when the light is transmitted from the upper surface, upward optical

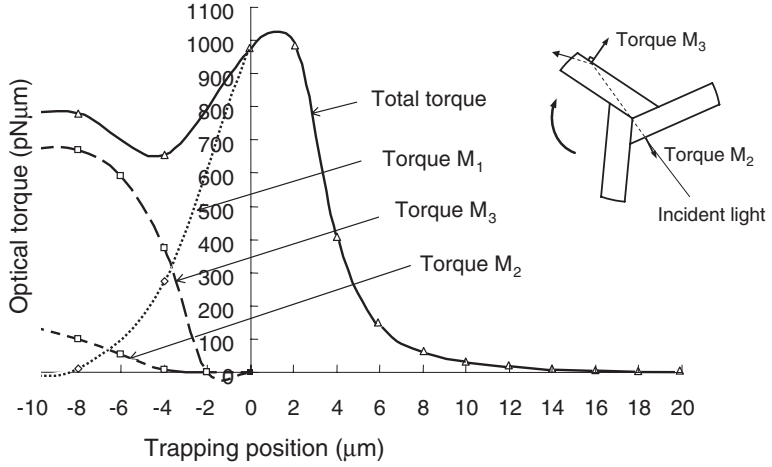

Fig. 3. Optical torque dependence on the trapping position for M_1, M_2, M_3, and $M_{\text{total}}^{\text{opt}} = M_1 + M_2 + M_3$ simulated for an SU-8 rotor under the conditions listed in Table 1.

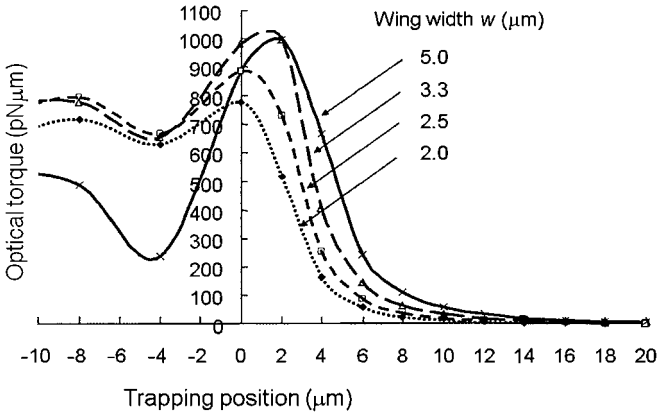

Fig. 4. Optical torque $M_{\text{total}}^{\text{opt}}$ dependence on trapping position with wing width as a parameter.

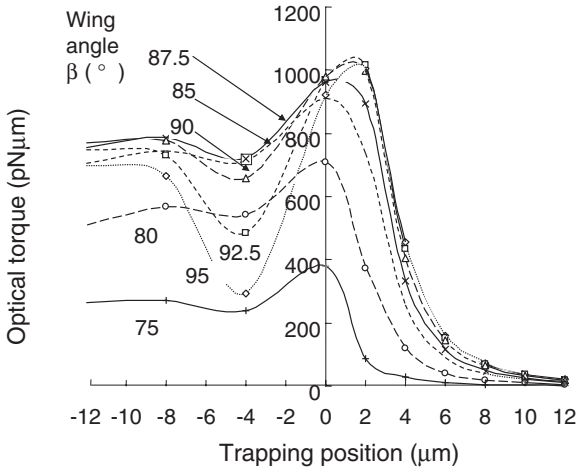

Fig. 5. Optical torque $M_{\text{total}}^{\text{opt}}$ dependence on trapping position with wing angle as a parameter.

Table 1. Conditions for optical torque simulation.

Laser power P (mW)	200
Objective lens NA	1.4
Refractive index of the immersion oil	1.52
Refractive index of the medium n_1	1.33
Refractive index of the mixer n_2	1.6
Rotor diameter d (μm)	20
Rotor thickness t (μm)	10
Speed of light in vacuum c_0 (m/s)	3.0×10^8

pressure force F_u is exerted. The total trapping force F_{total} is given by the sum

$$F_{\text{total}} = \iint (F_l + F_u) dS. \tag{4}$$

The trapping position is estimated from

$$F_{\text{total}} = (\rho - 1)Vg, \tag{5}$$

where ρ is the density, V is the volume of the rotor, and g is the gravitational acceleration.

For the calculation of F_{total}, the following three kinds of optical pressure are evaluated to obtain $F_{\text{total}} = F_l + F_u$ and $F_u = F_u{}^1 + F_u{}^2$.

1. Optical pressure F_l due to the light incident at the lower surface of the rotor.
2. Optical pressure $F_u{}^1$ due to the light incident at the lower surface and transmitted from the upper surface.
3. Optical pressure $F_u{}^2$ due to the light incident at the side surface and transmitted from the upper surface.

3.2 Wing width dependence on trapping position

Figure 6 shows the relationship between the trapping position and the optical pressure forces, F_l at the lower surface, F_u at the upper surface, total F_{total}, and $(\rho - 1)Vg$ due to the weight minus buoyancy for the SU-8 rotor of $d = 20\,\mu\text{m}$, $t = 10\,\mu\text{m}$, $w = 3.3\,\mu\text{m}$, and $\rho = 1.2$. The actual trapping position is defined as the value at the intersection between the total optical pressure F_{total} curve and the gravitational force $(\rho - 1)Vg$ line, giving $-7.6\,\mu\text{m}$, which agrees well with the experimental value (see Appendix).

It is also found from the figure that as the trapping position becomes a more negative value (moves in the rotor), incident light at the side surface increases (positive optical pressure at the upper surface increases), but the incident light at the lower surface decreases (negative optical pressure at the lower surface decreases), leading to rotor lifting.

Table 2 lists the trapping positions for the 3-wing SU-8

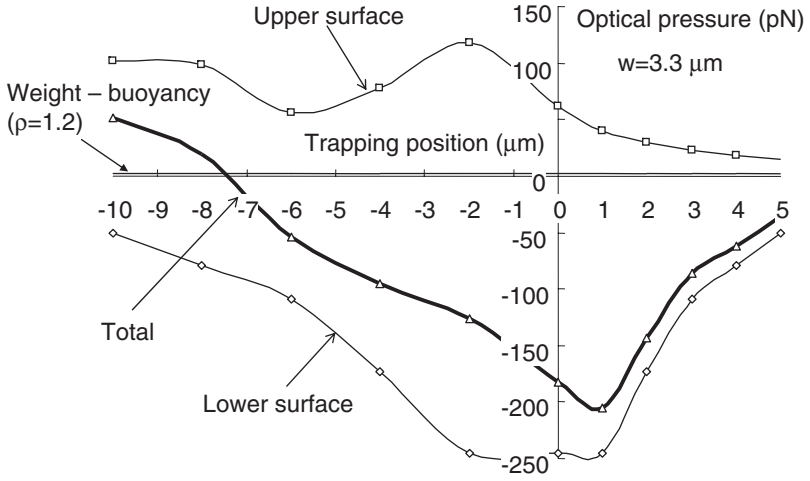

Fig. 6. Relationship between the trapping position and the optical pressure forces and the gravity minus the buoyancy for an SU-8 rotor (density $\rho = 1.2$ of diameter $d = 20\,\mu\text{m}$, thickness $t = 10\,\mu\text{m}$, and wing width $w = 3.3\,\mu\text{m}$.

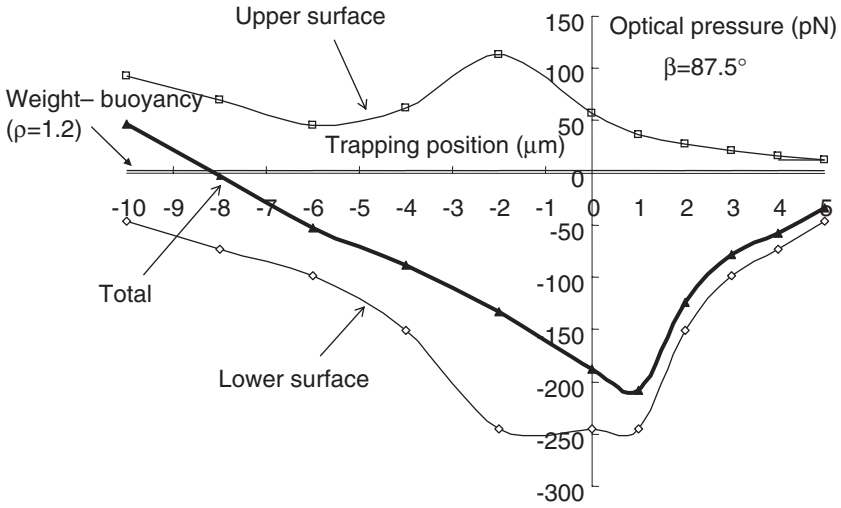

Fig. 7. Relationship between the trapping position and the optical pressure forces and the gravity minus the buoyancy for the rotor with a wing angle of 87.5°. Trapping position becomes $-8.0\,\mu\text{m}$ in the rotor.

Table 2. Relationship between wing width and trapping position for 3-wing SU-8 rotors at a laser power of 200 mW in water.

Wing width (μm)	Gravity (pN)	Trapping position (μm)
2.0	1.24	−9.0
2.5	1.56	−8.6
3.3	2.09	−7.6
5.0	3.24	−5.4

$P = 200\,\text{mW}$, $\rho = 1.2$.

Table 3. Relationship between wing angle and trapping position for 3-wing SU-8 rotors at a laser power of 200 mW in water.

Angle β (deg)	Gravity (pN)	Trapping position (μm)
80.0	1.48	−9.6
85.5	1.77	−8.6
87.5	1.93	−8.0
90.0	2.09	−7.6
92.5	2.26	−7.1
95.0	2.43	−7.0

$P = 200\,\text{mW}$, $\rho = 1.2$.

($\rho = 1.2$) rotor ($d = 20\,\mu\text{m}$, $t = 10\,\mu\text{m}$) with different wing widths at a laser power of 200 mW in water.

3.3 Wing angle dependence on trapping position

Figure 7 shows the relationship between the trapping position and the optical pressure forces, F_l at the lower surface, F_u at the upper surface, total F_{total} and $(\rho - 1)Vg$ for the rotor ($d = 20\,\mu\text{m}$, $t = 10\,\mu\text{m}$, and $w = 3.3\,\mu\text{m}$) with the wing angle of 87.5°. The trapping position becomes $-8.0\,\mu\text{m}$. Table 3 lists the trapping positions for 3-wing SU-8 ($\rho = 1.2$) rotors with different wing angles at a laser power of 200 mW in water.

4. Analysis of Fluidic Characteristics

4.1 Computational fluid dynamics (CFD)

To evaluate the performance of the optical rotor in water, the viscous drag force acting on the surface of the rotor was investigated by CFD.[17] We solved the continuity equation and the Navier-Stokes equation in a 3D geometry with a commercial CFD tool (Fluent, Fluent Asia Pacific Corp.). The control volume is a cube and each domain has a set of discretized equations that are formulated by evaluating and integrating the fluxes across the faces of the volume to satisfy the equations.

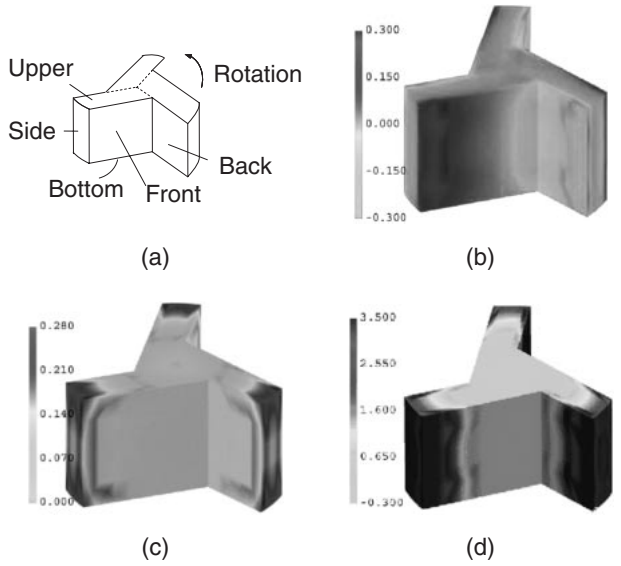

Fig. 8. (a) Parts names, (b) pressure P, (c) shearing stress S, and (d) drag force M_{drag} on the surface of the rotor at a rotation rate of 500 rpm.

The solver runs through a number of iterations to minimize the overall change in the selected parameters. If the error is below a prescribed value, the iteration process is terminated. Otherwise, we continue the iteration and obtain the pressure P and velocity $\boldsymbol{U}$ for each volume.

4.2 Drag force

Figure 8 shows (a) the parts names, (b) pressure P, (c) shearing stress S, and (d) drag force M_{drag} on the surface of the rotor at the rotation rate of 500 rpm. A high pressure is generated on the outer part of the wing where the fluid velocity is high. Flow-in occurs near the back surface because of the negative pressure. On the other hand, the shearing stresses are large on the side surface and on the outer corner. As a result, the drag force is large at the side surface and the outer parts of the back surface.

The viscous drag force M_{drag} acting on the surface of the rotor because of the pressure (normal component) and the shearing stress (tangential component) on all the surfaces is evaluated as

$$M_{\mathrm{drag}} = \iint r^2(P_{\mathrm{t}} + S_{\mathrm{t}})dr\,d\theta, \tag{6}$$

where P_{t} is the torque component of pressure P, S_{t} is that of the shearing stress, and r is the radius at that point. The parameters used in the analysis are the wing width w and the wing angle β of the rotor with a 20 μm diameter.

Figure 9 shows the drag force of different parts of the rotor at the rotation rate of 500 rpm. As the wing width increases, the surface areas of the side, upper and bottom increase, leading to an increase in the drag force of those parts, but the surface areas of the front and back decrease, leading to a decrease in the drag force of those parts. Figure 10 shows the total drag force of the rotor at the rotation rate of 500 rpm, with wing width as a parameter. It is found that the total drag force is constant (about 800 pN μm) for the wing width less than 5 μm.

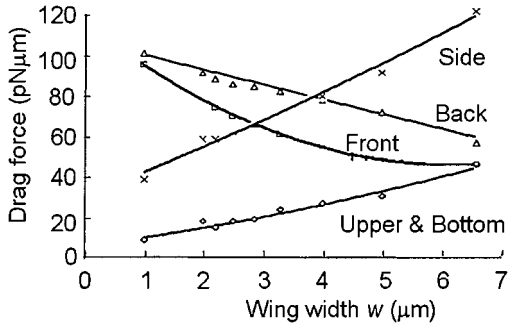

Fig. 9. Viscous drag force dependence on wing width for various rotor parts.

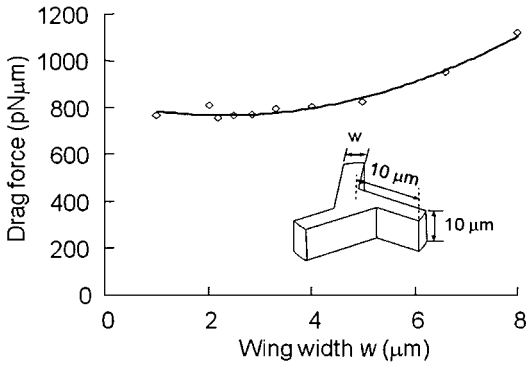

Fig. 10. Total drag force dependence on the wing width of a 3-wing optical rotor with $d = 20\,\mu\mathrm{m}$, $t = 10\,\mu\mathrm{m}$ and $w = 3.3\,\mu\mathrm{m}$.

5. Rotation Rate Considering the Trapping Position

5.1 Rotation rate analysis

The rotation rate is adjusted by balancing the total optical torque $M_{\mathrm{total}}^{\mathrm{opt}}$ with the drag force M_{drag}, which is linearly proportional to the rotation rate. Figure 11 shows the rotation rate dependence on the trapping position at a laser power of 200 mW with wing width as a parameter. The rotation rate is high for narrow wings of $w = 3.3$ and 2.5 μm when the trapping position is in the rotor. Figure 12 shows the rotation rate dependence on the trapping position at 200 mW with wing angle as a parameter. When trapped in the rotor, the rotation rate is high at wing angles less than 90°.

5.2 Wing width dependence of rotation rate

Figure 13 shows the rotation rate dependence on the wing width at 200 mW in water considering the trapping position obtained as listed in Table 2. The rotation rate is highest with the wing width of 2.5 μm for the 3-wing SU-8 rotor of 20 μm diameter and 10 μm thickness. It is also seen from the figure that theoretical rotation rates agree well with experimental values.

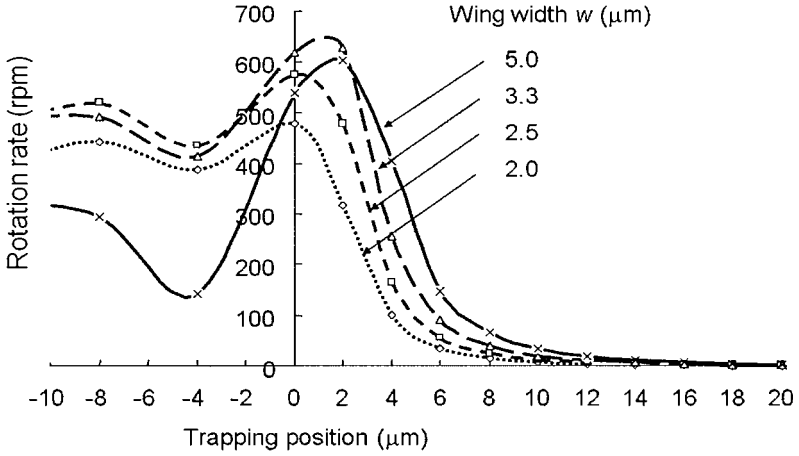

Fig. 11. Rotation rate dependence on trapping position in water at a laser power of 200 mW with wing width as a parameter.

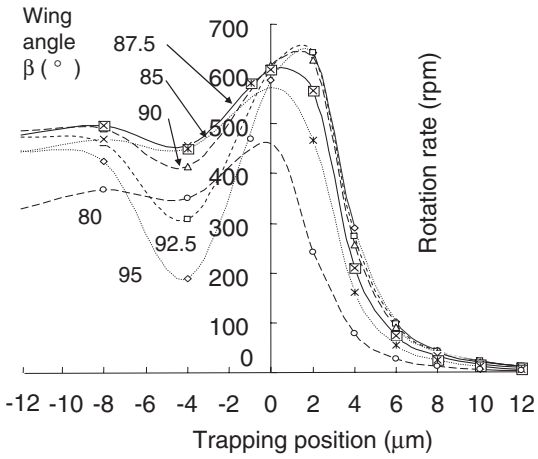

Fig. 12. Rotation rate dependence on trapping position in water at 200 mW with wing angle as a parameter.

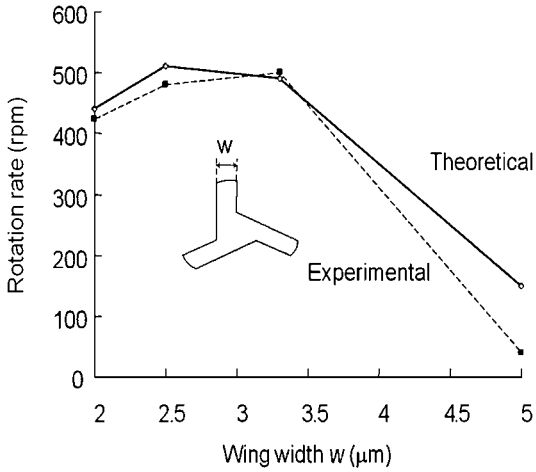

Fig. 13. Rotation rate dependence on wing width in water at 200 mW, considering the trapping position under the conditions listed in Table 2.

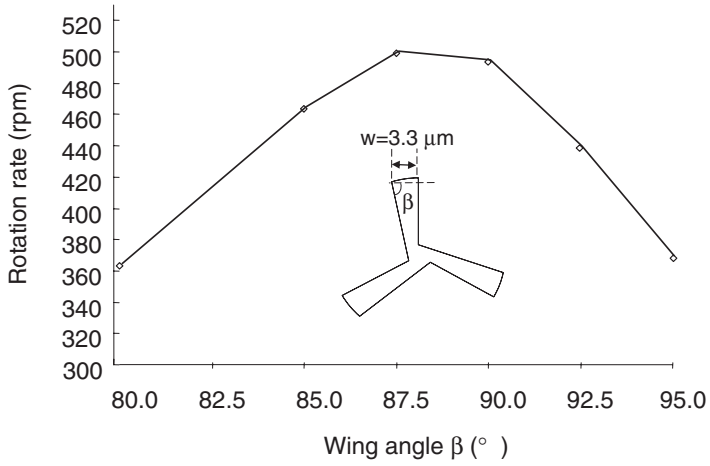

Fig. 14. Rotation rate dependence on the wing angle, considering the trapping position listed in Table 3, at the laser power of 200 mW in water.

5.3 Wing angle dependence of rotation rate

Figure 14 shows the rotation rate dependence on the wing angle at 200 mW in water considering the trapping position listed in Table 3. The rotation rate is highest at the wing angle of 87.5° for the 3-wing rotor of 3.3 μm wing width, 20 μm diameter and 10 μm thickness.

6. Conclusions

The performance of a light-driven 3-wing rotor with upward-directed focused beam illumination was analyzed using not only a ray optics model to obtain the optical torque and the trapping position, but also computational fluid

Table 4. Relationship between wing angle and drag force for 3-wing rotors at 500 rpm in water.

Angle β (deg)	Drag force (pN μm)
80.0	772
85.0	784
87.5	789
90.0	793
92.5	791
95.0	783

3-wing, 500 rpm.

dynamics (CFD) to evaluate the drag force and then to simulate the rotation rate.

First, to obtain the optical torque when the trapping position is in the rotor, not only the ray incident at the lower surface but also that at the side surfaces of the rotor are considered, with wing width and wing angle as parameters. Optical torque 1 due to the ray incident at the lower surface and transmitted from the side surface, optical torque 2 due to the ray incident at a wing side surface and transmitted from the same side surface, and optical torque 3 due to the ray incident at a wing side surface and transmitted from another wing side surface were computed and summed to obtain the total optical torque.

It was found that as the trapping position increases in the rotor, optical torque 3 increases rapidly, playing an increasingly important role. The total optical torque is large for both a narrow wing and a wing angle less than 90° when the trapping position is in the rotor, that is, for upward-directed illumination, but large for both a wide wing or a wing angle greater than 90° when the trapping position is placed outside the rotor.

Second, the trapping position was determined by balancing the total (both at the lower and the upper surfaces) optical pressure and the weight (minus buoyancy) in water for the SU-8 rotor with 20 μm diameter and 10 μm thickness. It was confirmed that the trapping position is in the rotor with the upward-directed focused laser beam illumination, and that this position increases in the rotor as the wing width or the wing angle decreases.

Third, the viscous drag force acting on the surface of a rotor was analyzed using CFD by integrating the torque components due to the pressure and the shearing stress on all surfaces of the rotor. It was found that the total drag force is about 800 pN μm for the wing width less than 5 μm thick at 500 rpm. Then the rotation rate is simulated by balancing the total optical torque with the drag force.

Finally, enhanced rotation rate shapes were demonstrated with various wing widths and wing angles, the optimum ones being a 2.5 μm wing width or 87.5° wing angle for the 3-wing rotor of 20 μm diameter and 10 μm thickness.

Acknowledgement

The authors would like to thank Professor Y. Ogami of Ritsumeikan University for his help with the computational fluidic dynamics.

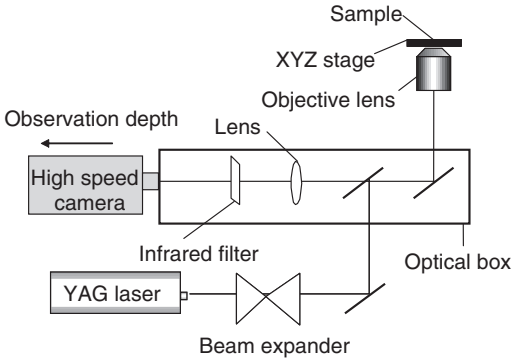

Fig. A·1. Experimental setup to measure the trapping position and the rotation rate of a 3-wing rotor. The upward-directed YAG laser traps the rotor inside, as described in §3.

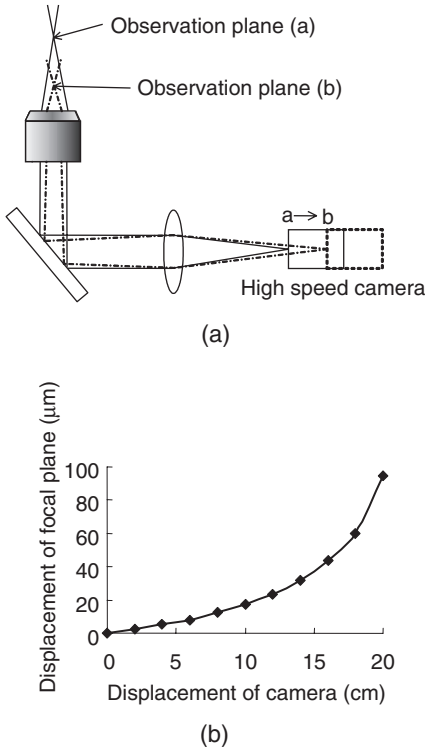

Fig. A·2. Measurement method of the trapping position (a), and displacement relationship between y of a high-speed camera and x of the focal plane (b).

Appendix

The trapping position was measured as follows. Figure A·1 shows the experimental setup for trapping and rotating the rotor with an upward-directed YAG laser beam and for observing the rotor using a high-speed camera. The rotor in water inside the chamber was secured at the focal point (trapping position) of the objective lens. Since the focal point is inside the rotor, at a distance x from the lower surface, the lower surface looks blurred on the monitor screen. The distance x was measured by moving the image plane of the camera from the focal plane to the lower surface, with a high-speed camera placed at a distance

y along the optical axis. The pre-observed relationship between *x* and *y* is shown in Fig. A·2.

References

1) K. Svobada, C. F. Schmidt, B. J. Schnap, and S. M. Block: Nature **365** (1993) 721.
2) ed. H. Masuhara: *Microchemistry* (Elsevier, Amsterdam, 1994).
3) A. Ishijima, H. Kojima, T. Funatsu, M. Tokunaga, H. Higuchi, H. Tanaka, and T. Yanagida: Cell **92** (1998) 161.
4) D. G. Grier: Nature **424** (2003) 810.
5) M. E. J. Friese and H. Rubinsztein-Dunlop: Appl. Phys. Lett. **78** (2001) 547.
6) O. Hahtela and I. Tittonen: Appl. Phys. B **81** (2005) 589.
7) H. Ukita, K. Takada, and Y. Itoh: Proc. SPIE **5514** (2004) 704.
8) S. Maruo and H. Inoue: Appl. Phys. Lett. **91** (2007) 084101.
9) S. Balslev, B. Bilenberg, O. Geschk, A. M. Jorgensen, A. Kristensen, J. P. Kutter, K. B. Mogensen, and D. Snakenborg: Tech. Dig. MEMS, 2004, p. 89.
10) E. Higurashi, R. Sawada, and T. Ito: Appl. Phys. Lett. **73** (1998) 3034.
11) S. J. Parkin, G. Knoner, T. A. Nieminen, N. R. Heckenberg, and H. Rubinsztein-Dunlop: Opt. Express **14** (2006) 6963.
12) R. C. Gauthier: Appl. Phys. Lett. **67** (1995) 2269.
13) E. Higurashi, H. Ukita, H. Tanaka, and O. Ohguchi: Appl. Phys. Lett. **64** (1994) 721.
14) P. Galajda and P. Ormos: Appl. Phys. Lett. **78** (2001) 249.
15) H. Ukita and K. Nagatomi: Appl. Opt. **42** (2003) 2708.
16) H. Ukita, K. Takada, D. Akagi, T. Ohnishi, and Y. Nonohara: IEEJ Trans. Sensors Micromach. **127** (2007) 25 [In Japanese].
17) H. Ukita: *Micromechanical Photonics* (Springer, Berlin, 2006).